Research Article | Vol. 30, No. 4 / 14 Feb 2022 / Optics Express 5937

Optics EXPRESS

Analyzing light-structuring features of droplet lenses on liquid-repelling surfaces

VALERIIA BOBKOVA,[1,*] SARAH TRINSCHEK,[2] EILEEN OTTE,[1] AND CORNELIA DENZ[1]

[1] *Institute of Applied Physics, University of Muenster, Corrensstr. 2/4, 48149 Münster, Germany*
[2] *Department of Engineering Physics, Münster University of Applied Sciences, Stegerwaldstr. 39, 48565 Steinfurt, Germany*
[*] *v.bobkova@uni-muenster.de*

Abstract: The complete understanding of the formation of seemingly levitating droplets on liquid-repelling surfaces provides the basis for further development of applications requiring friction-free liquid transport. For the investigation of these droplets and, thereby, the underlying surface properties, standard techniques typically only reveal a fraction of droplet or surface information. Here, we propose to exploit the light-shaping features of liquid droplets when interpreted as thick biconvex elliptical lenses. This approach has the potential to decode a plethora of droplet information from a passing laser beam, by transforming the information into a structured light field. Here, we explore this potential by analyzing the three-dimensional intensity structures sculpted by the droplet lenses, revealing the transfer of the characteristics of the underlying liquid-repelling effect onto the light field. As illustrative complementary examples, we study droplet lenses formed on a non-wetting Taro (*Colocasia esculenta*) leaf surface and by the Leidenfrost effect on a heated plate. Our approach may reveal even typically "invisible" droplet properties as the refractive index or internal flow dynamics and, hence, will be of interest to augment conventional tools for droplet and surface investigation.

1. Introduction

Droplets that are conveyed almost without friction over surfaces enable a unique transport mechanism of liquids, contributing to the advancement of a wide range of applications, as for instance, self-cleaning, drop-wise condensation, anti-icing, or mobility in microfluidic lab-on-a-chip systems (see refs. [1,2] and refs. therein). These so-called levitating droplets are formed on surfaces due to different liquid-repelling properties originating from the micro-, nano-, or hierarchical structure of the natural or artificial surface [3–7], chemical properties as high electronegativity of fluoropolymer coatings [8,9], thermal effects as the Leidenfrost effect [10,11], or a combination of these. Taking advantage of the mentioned surface properties, researchers have created, for instance, adaptable liquid lenses, tunable by e.g. dielectrophoretic forces or electro-wetting [12–14] thereby contributing to the advancement of novel electrotunable and optoelectronic devices. To further advance these applications, it is indispensable to gain a deeper understanding of the underlying liquid-repelling effects, which can be accessed by a detailed knowledge of the features of the droplets formed by them.

The investigation of droplets formed on surfaces is typically based on standard imaging systems, partially of high resolution and/or at high speed, and a subsequent image analysis. For instance, the surface wettability can be characterized by the contact angle at the interface where liquid, air and solid surface meet [15]. The contact angle measurement is typically performed by observing the droplets from the side by a standard imaging system. In this case, the contact angle is determined by, for example, sessile-drop goniometry analyzing video images of the droplets

#444777 https://doi.org/10.1364/OE.444777
Journal © 2022 Received 4 Oct 2021; revised 19 Dec 2021; accepted 20 Dec 2021; published 9 Feb 2022

Optics EXPRESS

by a fitting procedure [15,16]. The tilting-plate method [17] exploits the relation between the sliding angle and the contact angle. The sample is tilted gradually to find the sliding angle at which the droplet starts to move. To draw conclusions about the properties of the droplets and the surface, it is formed on, these methods analyze a two-dimensional (2D) projection of the three-dimensional (3D) droplet, typically by calculating the contact angle, i.e. only a single property of the droplet. A third approach takes advantage of the coherence of laser light [18], interfering a significantly expanded beam, passing through the droplet and its surrounding, with a reference beam to subsequently analyze the interference pattern. This holographic approach allows investigating temperature changes in the vicinity of the droplet, but does not reveal explicit properties of the droplet itself.

In contrast, for in-depth understanding of the fundamental effects behind the formation and dynamics of droplets on non-wetting surfaces, and particularly for future applications as liquid lenses, further droplet properties beyond the contact angle and surrounding temperature changes are of crucial interest. Among them are the complete 3D shape of the droplet, the density of the liquid, its refractive index or its dynamic behavior.

We propose implementing laser light to advance standard 2D imaging by encoding a multitude of droplet information into a Gaussian beam passing through the droplet. More precisely, we study the light-structuring properties of levitating droplets on liquid-repelling surfaces (substrates), exploiting their action as biconvex liquid droplet lenses to fully structure the passing light. The resulting beam will be shaped three-dimensionally in its amplitude and phase by the droplet, and hence, a structured light field [19–21] is formed with its spatial properties containing information on the droplet and, thereby, substrate characteristics. Structured light is known as a powerful information carrier since modulating its amplitude, phase, and also polarization allows encoding information in an effective way [19]. These degrees of freedom are not only sensitive to, for instance, the 3D shape of the droplet, i.e. the liquid lens, but also its refractive index and temporal shape changes. Beyond, since structured light also allows accessing the longitudinal and transverse Doppler shift [22,23], it additionally paves the way to detect internal flow dynamics.

Though light-shaping features of droplets have been studied previously, in these cases, droplets are not located on a substrate but are levitated by, e.g., an ultrasonic levitator (acoustic trapping) or the light passes through the droplet perpendicular to the substrate. In the former case, droplets sculpt sophisticated caustic structures [24,25] and droplet properties can be extracted by studying the inter-caustic scattering [26–28]. However, characteristics of the substrate below the droplet cannot be evaluated, since a substrate disturbs the formation of caustic light patterns and, thus, its subsequent analysis. In the studies based on perpendicular transmission through a droplet, the light also interacts with or passes through the substrate itself and experiences only a single curved drop-air interface passage, similar to a plano-convex lens. Thus, the propagation distance through the liquid does not directly influence the resulting structured light field, but the light is solely shaped by the properties of the curved interface. In recent works, these droplets are, for example, considered as liquid lenses of adaptable shape and focal length [14,29]. In contrast, in our approach, the beam passes through the droplet parallel to the solid substrate such that the passing beam experiences two curved drop-air interfaces, similar to a biconvex lens, and is sculpted by the complete 3D shape as well as by the propagation path through the liquid droplet lens. Additionally, droplet characteristics as its refractive index and its dynamic behavior, which depends on the implemented liquid-repelling effect, will be transferred to the passing light.

To study the ability to encode different droplet information into structured light, we investigate the 3D light-shaping characteristics of biconvex elliptical liquid droplet lenses formed by two different exemplary liquid-repelling effects and compare them to light focusing by a glass ball lens. For this purpose, in Section 2., we first introduce our experimental concept as well as the numerical approach used to support our experimental data, whereby we analyze the light intensity structured by a ball lens. Subsequently, on the one hand, the non-wetting characteristic

Optics EXPRESS

of a Taro leaf (*Colocasia esculenta*) is used, enabling the formation of droplet lenses due to its super-hydrophobic surface structure of micro- and nano-sized bumps that are coated with a waterproof wax [6,30]. The light-shaping features of these droplets are presented in Section 3.. On the other hand, we take advantage of the Leidenfrost effect on heated surfaces, creating levitating droplets due to an isolating steam layer between the surface and the liquid [10]. We present the respective 3D light-shaping properties in Section 4.. Even though the formed droplets for both effects are of similar, approximately ellipsoidal shape, the underlying liquid-repelling effects reveal characteristic features and transmit them to the droplet lenses. Droplets formed on the super-hydrophobic Taro leaf are rather stable in shape, only evaporating slowly at room temperature and showing no significant dynamics. In contrast, Leidenfrost droplets are less stable, revealing complex nonlinear dynamic high-speed changes of their shape due to a lack of friction, quicker evaporation, strong internal flow dynamics, and temperature gradients, which we demonstrate by experiments in Section 4.2 and support by numerical simulations in Section 4.3. Our results highlight these characteristics of the exemplary effects and, thereby, pave the way to a deeper understanding of liquid-repelling effects by taking advantage of structured light as well as to next-generation applications of floating droplets.

2. Concept of light shaping by droplet lenses

To analyze the light-shaping properties of droplets on a Taro leaf as well as Leidenfrost droplets, we experimentally investigated the sculpted intensity structure was experimentally investigated behind the droplet lenses, i.e. in propagation direction of the input beam, and completed it by a numerical verification. We considered Droplets were considered to be in a size range of 1 to 2 mm in diameter. A Gaussian beam horizontally passes through and, thus, is scattered by the droplets, as sketched in Fig. 1(a). In general, a light field scattered by a droplet is formed by different effects, namely, refraction, diffraction, and internal reflections. However, the beam waist of the beam is chosen to be smaller than the droplet height to minimize diffraction effects from the droplet's surface and the substrate below the droplet. Additionally, in beam propagation direction, the contribution of light originating from internal reflections within the droplet is negligibly small in comparison to refracted light. The droplet lenses can be approximated by an ellipsoidal shape, and thus, be considered as thick, biconvex elliptical lenses, that are characterized by their three semi-axes, i.e. R_x, R_y and R_z. The light field and, thus, the intensity shaped by a biconvex droplet lens are mainly defined by the light refraction at the first and second air-liquid interface and the beam propagation through the liquid volume. Note that, due to the local curvature of ellipsoidal droplet surfaces, not only paraxial but also non-paraxial electric field components are created, contributing to the focal field behind the liquid lens.

First, the 2D or 3D intensity structure behind a liquid lens is experimentally studied, as outlined in Sec. 2.1. Subsequently, we use the experimental image of the droplet (side-view) is used to approximate its shape by an ellipse in order to verify the measured intensity structure via a numerical simulation. Note that droplets could also be approximated by more complex models [31–33] but, in the presented cases, an elliptical fit captures the experimentally recorded droplet shapes very well. The extracted parameters are applied in our numerical calculation of the focal intensity structure in the 3D volume, as explained in Sec. 2.2. In the following, we investigate the 3D intensity structure formed by a glass ball lens (2 mm diameter) is investigated as an illustrative example of our approach, since the ellipsoidal shape of low volume droplets on liquid-repelling surfaces typically approximates to a sphere (Sec. 3.1; Sec. 4.1).

2.1. Experimental system

The experimental system is depicted in Fig. 1(b). A linearly (horizontally) polarized Gaussian laser beam (wavelength $\lambda = 532$ nm) passes through a liquid droplet or glass ball lens with propagation direction parallel to the liquid-repelling surface. The surface is positioned horizontally, i.e.

Optics EXPRESS

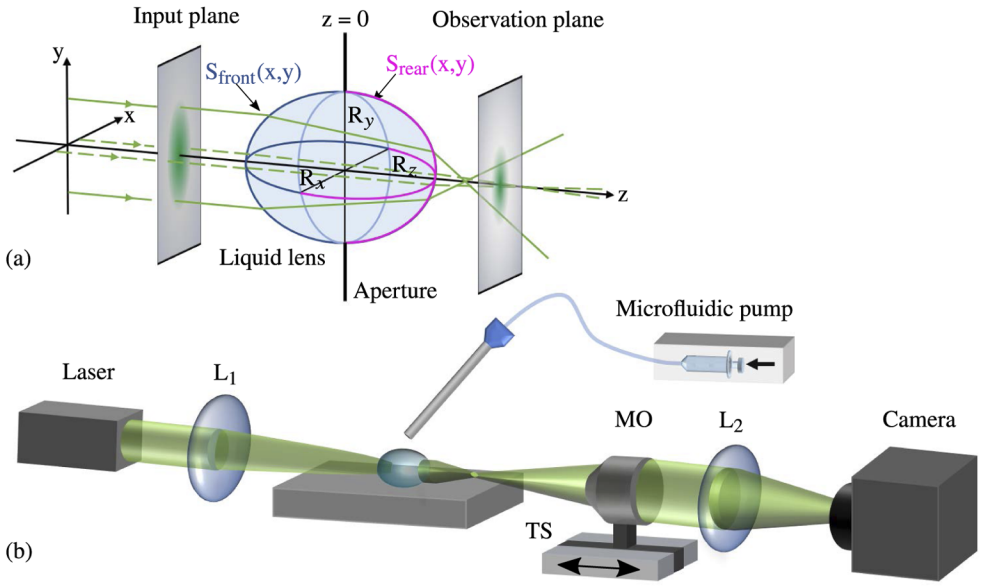

Fig. 1. Concept of shaping light by biconvex droplet lenses. (a) Beam propagation through the droplet lens and nomenclature applied in numerical simulation. The lens is defined by the interfaces $S_{\text{front}}(x, y)$ and $S_{\text{rear}}(x, y)$. If the lens is of approximately ellipsoidal shape, it is characterized by three semi-axes $R_{x,y,z}$. (b) Sketch of the experimental system used for analyzing the intensity structure shaped by liquid droplet lenses. Laser: horizontally polarized Nd:YAG, $\lambda = 532\,\text{nm}$, MO: 20× microscope objective with numerical aperture NA = 0.4, TS: translation stage, L_1: lens with focal distance $f = 400\,\text{mm}$, L_2: tube lens with focal distance $f = 200\,\text{mm}$, Camera: Ueye 1240-SE, pixel size $5.3 \times 5.3\,\mu\text{m}^2$. In order to obtain the 3D distribution of intensity structure the MO is shifted along the beam propagation direction (z-axis) by a high-precision TS.

orthogonal to the gravitational force. The Gaussian beam waist ($\omega_0 = 450\,\mu\text{m}$) is set to be at the position of the first interface of the liquid lens. Note that the respective Rayleigh range $z_r = 1.195\,\text{m}$ of the input beam tolerates slight mismatches of the position of the beam waist and the first drop-air interface, which are inevitable experimentally. In order to generate droplets of predefined volume spatially localized on a liquid-repelling surface, a microfluidic syringe pump with adjustable pumping rate and a blunt output cannula of 0.6 mm diameter is employed. The focused light is imaged onto a camera by a 20× microscope objective (MO) and a tube lens (L_2, focal distance $f = 200\,\text{mm}$). The MO is mounted on a motorized high precision z-shift stage (29 nm resolution), such that selected transverse (x, y)-planes at different z-positions can be imaged, enabling the detection of the discrete 3D intensity distribution. To achieve a high spatial resolution of our experimental results, we choose to record 500 (x, y)-planes to analyze the 3D light structures. Taking 500 images over 400 µm range takes 45 seconds. Droplet lens evaporation during that time is negligible for droplets on a Taro leaf, but not for droplets formed by the Leidenfrost effect. Hence, 3D intensity volumes for Leidenfrost droplets cannot not be obtained experimentally, but 2D distributions are investigated.

Exemplary experimental results of the 3D intensity distribution shaped by a ball lens with a diameter of 2mm and refractive index of $n = 1.458$ are illustrated in Fig. 2(a). We show t The distribution along the light propagation axis ((x, z)-plane) is shown as well as the exemplary distribution in four transverse planes (z_j, $j = [1, 4]$). Here and in the following, the (x, y) distributions are normalized to the maximum intensity in this particular plane. Moreover, the

Optics EXPRESS

line plots of the intensity are shown in Fig. 2(b), blue dots, normalized for each plane. Note that the experimental beam propagation axis does not perfectly match the z-axis of the translation stage. Therefore, the experimental values for the line plots, presenting the longitudinal intensity evolution, are taken along the tilted dash-dotted "intensity cut" line in Fig. 2(a), (x, z)-plane. To minimize aliasing effects due to the camera pixelation, the values for all line plots represent averaged values over two central pixel rows. The intensity distributions in Fig. 2(a), (b), demonstrate strong spherical aberration occurring due to the focusing of light by the spherical interfaces of the ball lens. The respective concentric intensity rings are observed in the transverse planes before the focal plane, i.e. position of highest intensity, (see z_1, z_2) and smooth rapid beam expansion behind the focal plane (see z_3, z_4). In the next step, we confirm our experimental results are confirmed numerically.

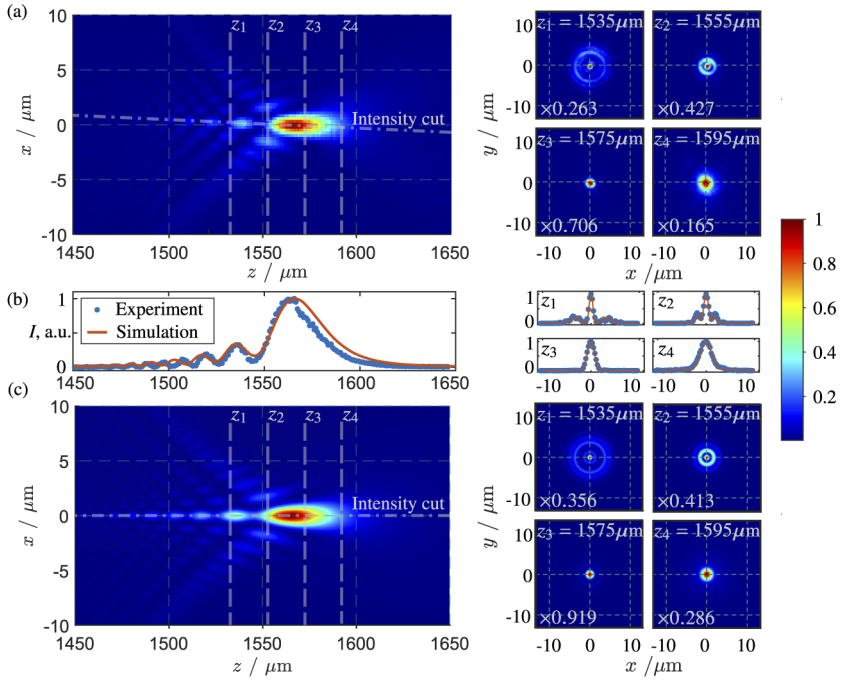

Fig. 2. Intensity structure shaped by a glass ball lens with 2 mm diameter. The (a) experimentally measured and (c) numerically calculated longitudinal as well as selected transverse intensity distributions are presented. The intensity in the (x, z)-plane is normalized to the maximal focal intensity I_f. The transverse intensity for the planes $z_j, j = [1, 4]$, is plotted on a scale normalized to the maximum intensity $I_{max}(z_j)$ in each plane. The respective scaling factors $I_{max}(z_j)/I_f$ are given within the images. The comparison between experiment and simulation is given by (b) line plots for longitudinal and transverse distributions (normalized). Longitudinal intensity evolution is presented along the dash-dotted intensity cut line in (a) and (c); transverse plots correspond to the distribution along the x-axis.

2.2. Numerical approach

In our experimental configuration, coherent laser light propagates in a non-paraxial manner through freely-shaped objects with physical dimensions much larger than the laser wavelength. These properties rule out many of the standard numerical techniques applied in optical simulations. Here, we use a vectorial ray-based diffraction integral (VRBDI) method introduced by Andreas et al. [34,35] is used to simulate the propagation of the Gaussian beam through the system and

Optics EXPRESS

thereby verify the experimental results. The VRBDI method was originally developed in the context of interferometry to simulate the propagation of a diffracting beam through an optical system. It combines vectorial diffraction theory, ray aiming, differential ray tracing and matrix optics to account for both, the geometrical shape of the optical system as well as diffraction effects [34]. The MATLAB source code for VRBDI was published online and can be downloaded from [36]. In principle, the method works as follows: Coherent monochromatic laser light is defined at an input plane and the electric field is spatially decomposed into its plane wave components. These components are represented by ray bundles (each consisting of five parallel rays), which are traced through the system that is described by the (smooth) surfaces of its optical components. The ambient medium (air) and the lens medium are hereby each assumed to be homogeneous and isotropic. At the interfaces of the components, the Fresnel equations are applied. Every point on a regular grid on the input plane is connected to the points on a defined intermediary plane placed shortly behind the lens via an iterative ray aiming algorithm. For an input plane sampled by $N_1 \times N_1$ pixels and an intermediary plane sampled by $N_2 \times N_2$ pixels, $N_1 \cdot N_2$ ray bundles are launched. At each point of the intermediary plane, the contributions of N_1 ray bundles (if not terminated before) are added coherently in amplitude and phase by an integral superposition. From the intermediary plane, the field is propagated to an observation plane at a given z-position by numerically calculating vectorial diffraction integral (VDI) in free space. Note that the employed simulation method does not account for multiple internal reflections, surface waves and diffraction effects arising at the surface of the droplet. However, since the beam waist is chosen to be smaller than the droplet height, diffraction effects from the surface are small also in experiment.

Figure 1(a) schematically shows the simulation of a Gaussian beam refraction by a lens defined by its front and rear interfaces, $S_{\text{front}}(x, y)$ and $S_{\text{rear}}(x, y)$, respectively. Since the shape of the glass ball lens is known, there is no need to fit an experimental image of the lens for interface parameter extraction. However, for a liquid lens, this step is crucial for the definition of refracting surfaces (see following sections). For the glass ball lens, two spherical air-glass interfaces and a refractive index of 1.458 for the volume enclosed by the interfaces are used in the simulation. The Gaussian input beam is sampled by 51×51 pixels over 2mm $\times$ 2mm on the input plane and propagated to an intermediary plane with 251×251 pixels. The transverse intensity distribution is calculated for a number of observation planes with resolution of 151×151 pixels located at a distance z from the center of the lens with a z-spacing of 1 µm. On a desktop PC without employing parallelization, the computational time is in the order of one hour for propagation from the input plane to the intermediary plane and in the order of one minute for numerically solving the VDI to each observation plane at a given $z-$position.

The numerical results, presented in Fig. 2(c), confirm our experimental measurement as shown in Fig. 2(a). In order to compare the experimentally measured intensity distribution and the obtained simulation results, we also present intensity line plots for simulation results in Fig. 2(b), red curves. Line plots represent simulated values (normalized) along the z- (left) and x-axis (right). Plots for simulation and experiment are in good agreement. Minor deviations in both transverse and longitudinal line plots can be explained by camera aliasing effects and limited experimental z-shift precision. Experimental intensity values are averaged within a camera pixel ($5.3 \times 5.3\,\mu\text{m}^2$), corresponding to a $0.265 \times 0.265\,\mu\text{m}^2$ area in measurement planes behind the ball lens, considering $\times$20 MO magnification. In contrast, simulations have a transverse resolution of $0.134 \times 0.134\,\mu\text{m}^2$. Additionally, minimal experimental mismatch of the MO z-shift or the ball lens center and beam propagation axes limit the experimental accuracy. However, in total, the qualitative match between experiment and simulations confirm the eligibility of the employed simulation method.

Optics EXPRESS

3. Shaping light by droplet lenses on a Taro leaf

3.1. Droplets on super-hydrophobic surfaces

When a droplet is placed on a flat solid substrate, its shape is determined by the action of gravity and the tensions of the involved interfaces. The local contact angle the droplet forms with the substrate is given by the Young equation $\cos(\theta) = (\gamma_{sv} - \gamma_{sl})/\gamma_{lv}$, where γ_{sv}, γ_{sl} and γ_{lv} are the interfacial tensions of the solid-vapour, solid-liquid and the liquid-vapour interface, respectively [37]. A substrate is called hydrophobic if the contact angle θ is larger than 90°. If the substrate is extremely difficult to wet by a fluid and θ is larger than 150°, the substrate is called super-hydrophobic. This is often the case for micro-structured surfaces, with the most prominent example in nature being the leaf of the Lotus plant. The Lotus leaf shows a well-studied micro-pillar surface structure, which has inspired the creation of various functional, super-hydrophobic surfaces [38,39]. However, nature provides a multitude of other plants showing liquid-repelling behavior based on different micro-, nano-, or hierarchical structured surfaces and/or natural coatings [40]. A plant not showing the established pillar structure but still revealing excellent non-wettability is the Taro leaf (*Colocasia esculenta*). Only recently, the potential of Taro leaf characteristics for future technological applications has been disclosed by creating bio-inspired surfaces based on the leaf's morphology [6]. Its super-hydrophobic surface structure is composed of hexagonal microcavities with micro- and nano-sized bumps being coated with a waterproof wax. An exemplary photo of water droplets on a Taro leaf is presented in Fig. 3(a). For super-hydrophobic structured substrates, two wetting scenarios are possible: In the Wenzel state, the liquid is in intimate contact with the substrate [3]. In the Cassie-Baxter state, the droplet rests on top of the asperities [4]. The observed apparent contact angle of the droplet depends on the surface roughness and on the wetting state.

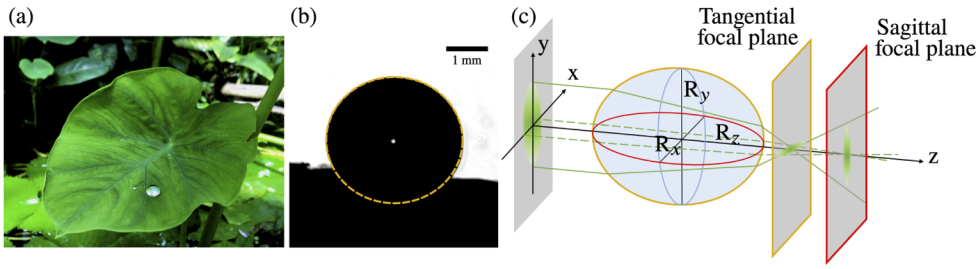

Fig. 3. Taro droplet lenses. Water droplets (a) on Taro leaf in nature and (b) in the experimental setting (side-view, blue background illumination, grayscale camera image; scale bar: 1 mm) with elliptical fit (orange). (c) 3D sketch of a droplet and ray tracing through it. Exemplary rays focusing in the tangential/ sagittal planes are shown as dashed/solid lines. Tangential/ sagittal focal plane as well as the respective refracting curvature are marked in orange/ red.

The relative importance of wetting and gravitational forces acting on the droplet can be characterized by the capillary length $l_c = \sqrt{\gamma_{sl}/(\rho g)}$, where ρ is the density of the fluid and g the gravitational constant. For small droplets with heights well below l_c, the influence of gravity can be neglected and the droplet shape is a spherical cap. For larger droplets, the flattening effect of gravity needs to be taken into account. The shape can be obtained by numerically integrating the Young-Laplace equation including hydrostatic pressure for a known droplet volume and a contact angle of a droplet [41].

Approximate droplet shapes can be obtained by assuming that the droplet takes on the form of an ellipsoid or, more precisely, an oblate spheroid with $R_x = R_z = R_{xz}$ and then determining the geometrical parameters of the model (e.g. the semi-axes of the spheroid) from a minimization

Optics EXPRESS

of the free energy [42,43] which consists of energetic contributions due to gravity and the inter-facial tensions at the liquid-substrate and liquid-vapour interface. Park et al. described large droplets on structured hydrophobic substrates in the Cassie-Baxter or Wenzel state by the overlapping geometry of double spheroids and verified the model predictions with experimental measurements on various micro-pillar arrays [31].

In our experiment we investigate distilled water droplets (refractive index $n = 1.33$) placed on a piece of a Taro leaf, fixed on a plane horizontal holder. We find that a fit by a simple oblate spheroid as depicted in Fig. 3(b) (scale-bar: 1 mm) describes the experimentally observed droplet shape reasonably well. Due to its symmetry, the spheroids are characterized by the two semi-axes R_y and R_{xz} (see Fig. 3(c)). For numerical calculations, these axes are extracted from the experimental images by a fit, as illustrated in orange in Fig. 3(b).

3.2. Focal intensity structures

Due to the spheroid shape of the droplet, we expect astigmatic focusing for droplet lenses on a Taro leaf, as sketched in Fig. 3(c). The two characteristic semi-axes R_y and R_{xz} of the droplet give two different curvatures in vertical (orange; elliptical fit) and horizontal (red; circular fit) direction, respectively. As a result, the focal distance for the tangential (orange) and the sagittal (red) planes differ, leading to astigmatic aberration. As outlined above, the semi-axes and, thus, the focal field shape are defined by the characteristics of the droplet liquid as well as the non-wetting surface.

We investigate thus the focusing properties of a water droplet formed on the surface of a Taro leaf. The shape of an exemplary water droplet is presented in Fig. 3(b). The corresponding experimental results for the 3D shaped intensity structure are presented in Fig. 4(a), illustrating the longitudinal (left) and transverse (right) intensity distributions. Following our expectations, two focal planes can be found, where the intensity is confined into a horizontally (tangential plane) or vertically (sagittal plane) elongated focal intensity line ($z_{2,5}$). Caused by spherical aberration, intensity fringes are formed shortly before these focal planes. These fringes are aligned with the following focal intensity line ($z_{1,4}$). After the tangential plane, the focal intensity lines expand in vertical y-direction, whereas it starts to narrow in horizontal x-direction to form the subsequent focal line in the sagittal plane. The ratio of R_{xz} and R_y affects the ratio of these intensity maxima as well as their longitudinal distance on the propagation axis. Since $R_{xz} > R_y$ for the oblate droplet, the refracting surface curvature corresponding to the tangential plane is stronger and the respective numerical aperture (NA) is higher than the one for the sagittal plane. Hence, the maximal intensity in the tangential plane is higher than that in the sagittal plane. From the side image of the droplet presented in Fig. 3(b), we approximate its elliptical shape in order to verify the measured intensity structure with a VRBDI simulation. This is performed using the open-source image processing library scikit-image [44] by first detecting the edges in the image via a Canny filter and secondly employing a Hough transform. We extract the semi-axes $R_y = 1.44\,\text{mm}$ and $R_{xz} = 1.59\,\text{mm}$. In Fig. 4(b), the simulated intensity structure is shown for a Gaussian beam that passes though the droplet with its propagation axis being perfectly aligned with the center of the droplet. This simulation captures the overall shape of the intensity and in particular the position of the sagittal and tangential focal plane. However, the simulated intensity distribution is symmetric about the $z-$axis, whereas the experimentally measured intensity is tilted and has an asymmetric intensity structure reveals asymmetry. These deviations can mainly be attributed to the experimental beam axis not being perfectly aligned with the ellipse axis R_z of the droplet. This is confirmed by an exemplary simulation of a Gaussian beam passing through the droplet off-axis with offsets $\Delta y = 200\,\mu\text{m}$ and $\Delta x = 50\,\mu\text{m}$ presented in Fig. 4(c) which qualitatively matches the experimental results. Remaining differences might be caused by, e.g., small deviations of the droplet from the elliptical shape, due to gravitational effects, or a slightly imperfect beam shape in experiment.

Optics EXPRESS

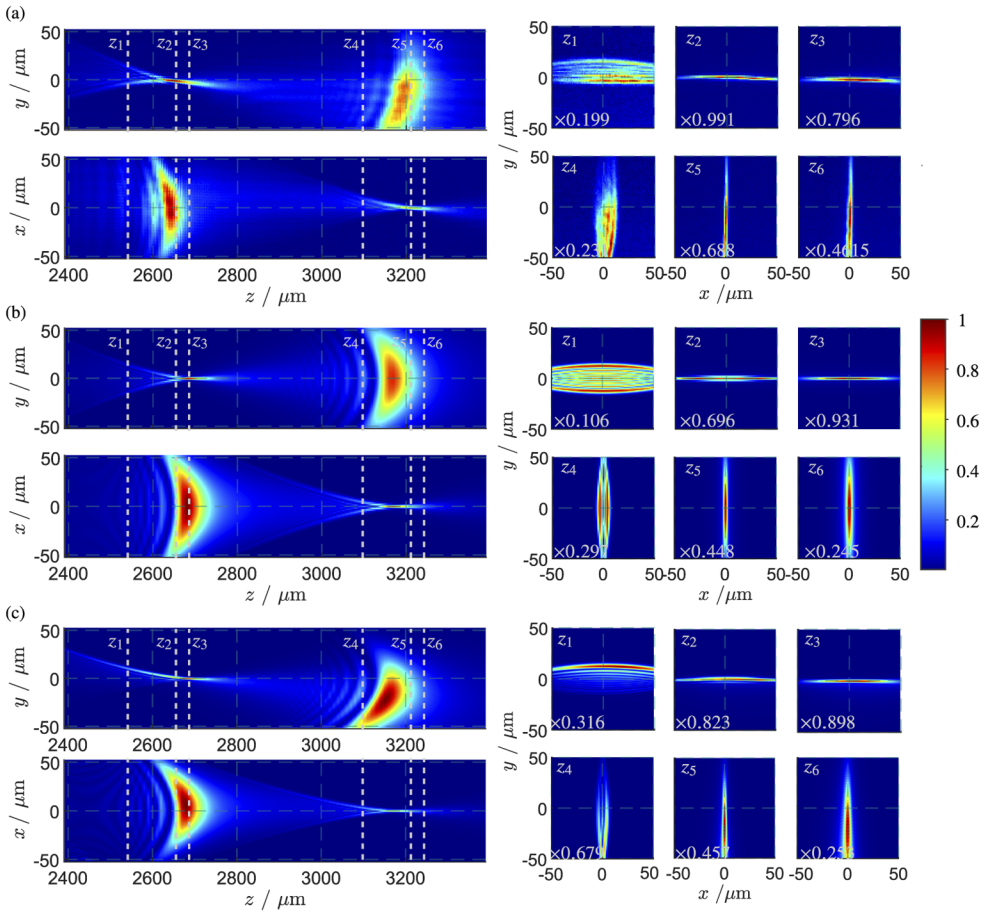

Fig. 4. Exemplary beam shaping by a droplet lens on a Taro leaf with $R_y = 1.44\,\text{mm}$ and $R_{xz} = 1.59\,\text{mm}$. The (a) experimentally measured and (b, c) numerically calculated longitudinal as well as selected transverse intensity distributions are presented. In (b), the optical axis of the Gaussian beam is aligned with the droplet center whereas in (c), an offset of $\Delta x = 50\,\mu\text{m}$ and $\Delta y = 200\,\mu\text{m}$ is assumed. The intensity in the (x, z)-plane and (y, z)-plane is normalized to the maximal focal intensity I_f. The transverse intensity for the planes $z_j = \{2550, 2660, 2690, 3100, 3210, 3242\}\,\mu\text{m}$, $j = [1, 6]$, is plotted on a scale normalized to the maximum intensity $I_\text{max}(z_j)$ in each plane. The respective scaling factors $I_\text{max}(z_j)/I_\text{f}$ are given within each image.

4. Shaping light by Leidenfrost droplet lenses

4.1. Leidenfrost droplets on heated surfaces

The second example of a biconvex droplet lens is formed by the Leidenfrost effect [10]. In this case, when a droplet is placed on a surface significantly hotter than the boiling point of the liquid, an insulating vapor film forms under the droplet, preventing the droplet from boiling and evaporating rapidly. Levitating above this liquid-repelling surface, the droplet is able to survive for up to several minutes before fully evaporating. In its equilibrium, the Leidenfrost droplet can be approximated by a spheroid, embedding a volumetric temperature gradient and related internal fluid flow dynamics [11,45]. Although the Leidenfrost effect is known for more than 250 years, it is not yet fully understood due to the complexity of the spatio-temporal dynamics,

Optics EXPRESS

and attracts continuous interest with respect to its promising features for future applications [11,46–50]. For instance, the self-propulsion of a Leidenfrost droplet due to its strong internal flow [11] can be beneficial for devices implementing a heat-to-motion transfer [46]. Recently, the bouncing dynamics of Leidenfrost droplets have attracted particular topical interest [47–49], revealing e.g. the previously unknown "trampolining" of Leidenfrost droplets.

The slightly adapted experimental setup for analyzing the focusing behavior of Leidenfrost droplet lenses is depicted in Fig. 5(a). The volume of the droplets, placed on a heated copper plate, is defined by the pumping rate of a microfluidic pump (MP) and the diameter of a (blunt) cannula. We employ a 98% ethanol solution due to its relatively low boiling temperature. In order to spatially localize a typically self-propelled Leidenfrost droplet, the copper surface is structured as a ratchet trap of concentric grids, in analogy to ref. [51]. The ratchet is fixed on a heating plate (HP) with a thermopaste and set to 300 °C. The needle is placed at a minimal height of 2.5 mm above the heating plate, such that the droplet is still detaching from the cannula while its initial potential energy is minimized when it drops onto the surface. An exemplary image of a Leidenfrost droplet is shown in Fig. 5(b). Note that, in order to trap the droplet stably in the ratchet trap center, two ratchet periods are chosen to be bigger then the diameter of the droplet. We observe the droplet illuminating it by a blue LED (λ_{LED} = 405 nm) and imaging it with a high-speed camera (NX8-S2 IDT; 1000 fps, 8.68 × 8.68 µm^2 pixel size) from the side. Onto the same camera, we simultaneously image the transverse light intensity structure, shaped by passing through the droplet (see Fig. 5(a)). The magnification of the imaging system (1.12 μm per pixel for the light intensity) is defined by the ×20 MO and the teleobjective on the camera in a way, that dynamic behavior of the Leidenfrost droplet (see next section), which is transfered to the light field, can be completely captured on the camera chip. Compared to the camera exposure time (1 ms), the difference in propagation time for the two observation arms can be neglected.

4.2. Bouncing Leidenfrost droplet lenses

Even though the shape of the Leidenfrost droplet levitating above a heated surface can be approximated by a spheroid, the dynamics related to the Leidenfrost effect and, in particular, the initial potential energy of the droplet – when placing the drop onto the heated surface – strongly effects the evolution of the droplet's shape in time. Thus, the relative position of the droplet surface to the beam waist varies in a micrometer range, which is negligible compared to the Rayleigh range of the incoming beam (z_{r} = 1.195 m). In the Visualization 1 (see Supplementary Video Material), which is represented as a time lapse in Fig. 5(d), we demonstrate our observation of the high-speed dynamics of the droplet shape and the intensity structure sculpted by the respective dynamic droplet lens, namely, the evolution of an exemplary Leidenfrost droplet (top) and the respective light field intensity (bottom) in a selected (x, y)-plane ($z \approx 1320\,\mu$m) during a time span of Δt = 13 ms. Figure 5(c) depicts the respective droplet shape evolution by overlapping the contour of the outer droplet edge extracted from each experimentally captured camera frame; the corresponding point in time is color-coded (see colorbar below).

Although the changes in the shapes of the droplet may appear minor when the droplet is captured as a 2D image with a camera, its significance become apparent when the transmitted light field is examined. The light intensity not only reveals the bouncing behavior of the droplet on the heated surface, but also the changes in the 3D shape of the droplet lens. The approximately vertical bouncing of the droplet mainly originates from its initial potential energy that causes the droplet to expand in the vertical direction, enlarging its vertical semi-axis R_y while narrowing its horizontal axes R_{xz}, as visible in Fig. 5(c). Additionally, upon bouncing, the droplet also deviates from the rotational symmetric shape of a typical spheroid, as highlighted for t = 2 ms, Fig. 5(d). The blue and pink dashed lines represent two different elliptical fits of the left and right outer edge of the droplet, respectively. This asymmetry might also occur in the (x, y)-plane, which is invisible for the 2D projection onto the camera. Due to the overall bouncing behavior,

Optics EXPRESS

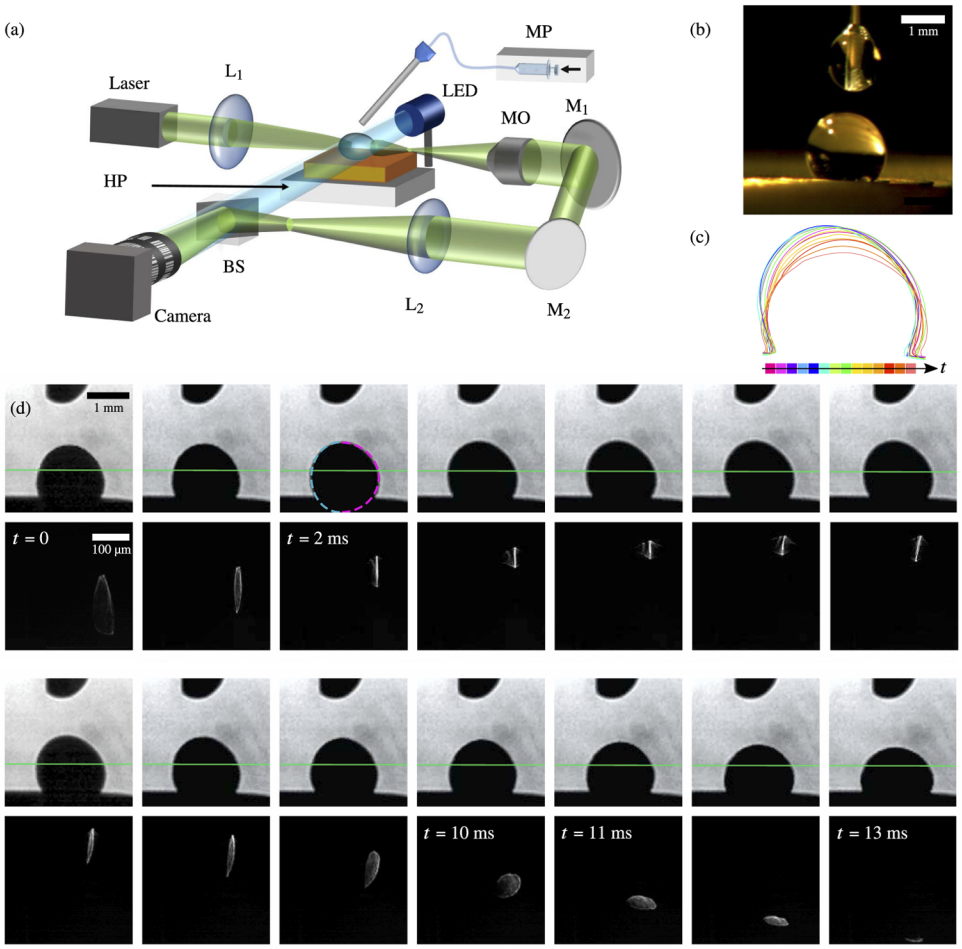

Fig. 5. Experimentally observed beam shaping by dynamic Leidenfrost droplet lenses. (a) Sketch of the experimental system which enables simultaneous observation of the Leidenfrost droplet shape (blue illumination) and the shaped intensity structure (green laser) with a single high speed camera (NX8-S2 IDT, up to 4000 fps, pixel size: 8.68 μm). L: lens; LED: light emitting diode, $\lambda_{\mathrm{LED}} = 405$ nm; MO: microscope objective; MP: microfluidic pump; M: mirror; BS: beam splitter; HP: heating plate. (b) Exemplary image of a Leidenfrost droplet lens in a ratchet trap (scale bar: 2 mm). (c) Color-coded time (t) evolution of the droplet shape within 13 ms. (d) Visualization 1 in the form of time lapse with 1 ms steps between camera frames shows the observed evolution of the droplet shape (top row; scale bar: 1 mm) and resulting transverse intensity structure (bottom row; scale bar: 100 µm). The propagation axis of the laser beam is indicated by the green horizontal line (propagation from left to right). The elliptical fit (blue/pink; $t = 2$ ms) corresponds to the numerical simulation in Fig. 6(d)

Optics EXPRESS

the propagation axis of the laser beam, sketched in green in (d), does not necessarily meet the center of the droplet lens or intersect with any of the droplets' semi-axes. As a consequence, the bouncing of the droplet lens becomes visible by a change in the transverse position of the observed intensity distribution (bottom rows in (d)), since the propagation direction of light changes accordingly when passing through the lens. The 3D bouncing dynamics of the droplet is encoded onto the passing light field, revealed in the horizontal and vertical position of the center of the observed intensity structure. Hence, the complex light field behind the droplet can unveil integral droplet information, invisible for a standard 2D side projection.

4.3. 3D intensity structures formed by the dynamic droplet lens

The dynamics of the Leidenfrost droplet and its respective 3D shape not only define the transverse position of the observed intensity distribution, but also sculpt the intensity distribution itself, as depicted in Fig. 5(d) (bottom rows). Particularly, we observe intensity lines (e.g. $t = \{6, 13\}$ ms), hyperbolic, or elliptical structures including intensity fringes or rings, respectively (e.g. $t = \{1, 11\}$ ms), defined by the shape of the focusing droplet surfaces and, caused by these, aberrations. The light structures resemble the observations for the astigmatic droplet lens formed on a Taro leaf (see Fig. 4). In contrast, for the Leidenfrost droplets, at specific times, the intensity lines as well as the ellipses are not aligned horizontally/ vertically, but are tilted. This tilting is related to the 3D shape of the droplet, what is confirmed when comparing to numerical calculations.

Note that, due to the extremely fast oscillation dynamics of the Leidenfrost droplet, experimentally, only a single transverse light intensity structure can be captured at a time. Thus, the 3D intensity structure formed after the droplet can only be obtained numerically by extracting the droplet shape from the image and simulating intensity distribution behind the liquid droplet lens.

Figure 6 shows numerical simulations of the longitudinal and transverse intensity distributions for Leidenfrost droplet lenses of different (y, z)-shapes extracted from the experimental images in Fig. 5(d) at (a) 10 ms, (b) 11 ms and (c) 13 ms. These images correspond to snapshots in the downward motion of the bouncing dynamics of the Leidenfrost droplet. From the extracted 2D elliptical droplet shapes, we approximate the 3D surface of the lens by a spheroid. Since previous experimental studies [11,45] showed that the temperature variations within the Leidenfrost droplet are limited to a few degrees, we assume the lens to have a homogeneous refractive index $n = 1.342$ for ethanol at the temperature $T \approx 60 \circ C$. For best illustration of the 3D intensity structures at different times, the origin of the numerical coordinate system is located at the center of the droplet, while the position of the propagation axis of the Gaussian input beam is shifted in height (see green line in Fig. 5(d)), neglecting possible shits in $\pm x$-direction. Hence, based on this offset, light propagation behind the droplet is characterized by an asymmetric focusing behavior in y-direction, which is confirmed by the longitudinal and selected transverse intensity images ($z_1 = 1320\,\mu$m, $z_2 = 1510\,\mu$m, and $z_3 = 1600\,\mu$m). Furthermore, the z-position of the tangential and the sagittal focal plane changes with the time-dependent ratio of the semi-axes R_y and R_{xz}. If the Leidenfrost droplet is almost spherical, both focal planes are approximately located at the same z-position (Fig. 6 (b)). If the droplet has the shape of a flat spheroid (Fig. 6 (c)), the tangential focal plane is located closer to the droplet than the sagittal focal plane. If the droplet is elongated in the vertical direction, the position of the focal planes is the other way around (Fig. 6 (a)).

Confirming our experimental observation close to z_1, the numerical transverse intensity distributions at z_1 not only reveal the expected asymmetry but also exhibit the elliptical or approximately line-like intensity distributions with intensity fringes due to spherical aberration. In general, from z_1 to z_3, the variation between vertically and horizontally extended light structures and fringes (no fringes) before (behind) tangential (sagittal) plane resembles the focusing behavior of droplet lenses on a Taro leaf. Additionally, cusp-like intensity structures, as

Optics EXPRESS

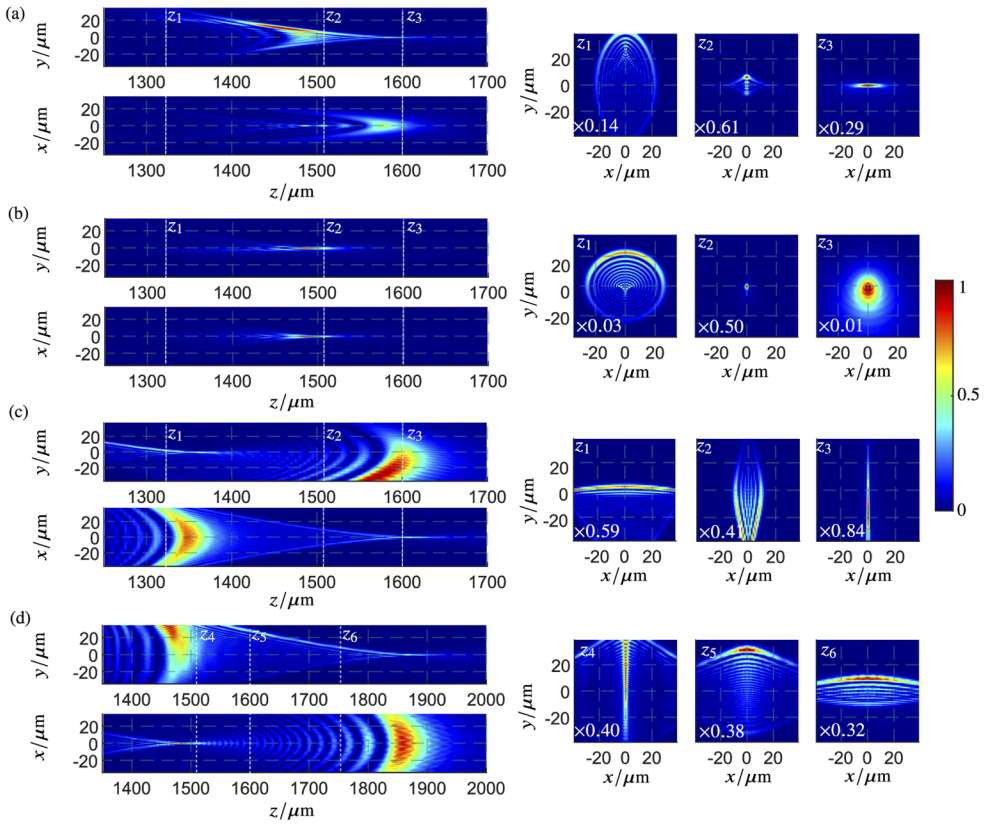

Fig. 6. Numerical investigation of Leidenfrost droplet lens properties. We show longitudinal (left) and transverse (right) intensity distributions for droplet lenses with semi-axes (a) R_y = 0.77 mm, R_{xz} = 0.80 mm, (b) R_y = 0.78 mm, R_{xz} = 0.77 mm, (c) R_y = 0.75 mm, R_{xz} = 0.83 mm, and (d) R_y = 0.83 mm, $R_{xz,\text{front}}$ = 0.67 mm, $R_{xz,\text{back}}$ = 0.9 mm extracted from the experimentally observed droplet shapes at 10 ms, 11 ms, 13 ms and 2 ms, respectively (cf. Fig. 5(d)). The intensity in the (x, z)- and (y, z)-plane is normalized to the maximal focal intensity I_f. The origin of the $y-$axis is located at the droplet center. The transverse intensity for the planes z_j is plotted on a scale normalized to the maximum intensity $I_\text{max}(z_j)$ in each plane. The respective scaling factors $I_\text{max}(z_j)/I_f$ are given within the images.

known for non-parabolic lenses, can be found within the elliptical structures for $z_{1,2}$ in (a) and z_1 in (b). This characteristic is also observed experimentally, e.g. at t = [3, 5] ms in Fig. 5(d). For the flatter droplet in (c), a cusp-like shape of lower intensity can be seen below the high-intensity horizontal line. This structure is narrowing with increasing z, forming hyperbolic transverse structures with a cusp at its top and bottom, similar to the distribution in z_2, before creating the vertical focal line at z_3. Similar hyperbolic distributions are found at t = {1, 7, 8} ms in the experimental results.

However, the experimentally observed 2D droplet shapes captured by the camera in the (y, z)-plane cannot be approximated well by a single elliptical fit for all the shapes. For example, the droplet shape at 2 ms (cf. Fig. 5(d)) shows a different curvature for the front and rear droplet surfaces. To approximate its interface, we fit two separate ellipses to the front and back of the droplet in the (y, z)-plane and overlap the geometries of two half-spheroids to a joint interface (see blue/ pink dashed fit in Fig. 5(d), t = 2ms). The two spheroids have the same semi-axis

Optics EXPRESS

R_y in vertical direction but different semi-axis R_z in horizontal direction. The numerically obtained longitudinal and transverse intensity distributions for this geometry are presented in Fig. 6(d). Also in this case we observe an asymmetry in y-direction, due to the position of the beam propagation axis, as well as a line-like or hyperbolic transverse intensity distribution. Qualitatively, the presented results for symmetric and asymmetric droplets are similar. However, the combination of the interfaces of the asymmetric drop shifts the tangential and sagittal focal plane significantly in $+z$-direction compared to symmetric examples (see z-axis in Fig. 6(d)).

Note that the asymmetries and tilting in x-direction of the experimentally observed transverse intensity structures cannot be observed in the presented numerical results in Fig. 6. In the respective simulations, the droplet is assumed to be a symmetric 3D spheroid (in Fig. 6(a)-(c)) or combination of two 3D spheroids (in Fig. 6(d)) with semi-axes extracted from the captured 2D images of the bouncing droplet. Shifts between beam axis and ellipsoid center in $x-$direction are not accounted for in the presented simulations. In the experiment, however, offsets in $x-$direction and deviations of the droplet from a perfect ellipsoidal shape give rise to an asymmetric intensity distribution in x-direction (cf. Fig. 5(d)). This observation highlights the potential of our experimental approach to encode a majority of droplet information into the passing light.

5. Conclusion

We have proposed an advanced analysis approach to study the light-structuring properties of levitating droplets on liquid-repelling surfaces, exploiting their action as biconvex liquid droplet lenses. The presented method has the potential to encode a manifold of droplet information onto a passing light field. As illustrative examples, we experimentally investigated the 2D and/or 3D intensity structure created by droplet lenses which are formed on a non-wetting Taro leaf or by the Leidenfrost effect and provided numerical verification for our results. For droplets on a Taro leaf, we demonstrated a combination of spherical and astigmatic aberrations, resulting in a 3D intensity structure with two focal planes of orthogonal focal intensity lines. While droplets on a non-wetting Taro leaf are stable for the planar surface, Leidenfrost droplets show dynamic changes in their shape, deviating from an obsolete spheroid. We presented how these dynamics manifest in clear changes in the shaped intensity, e.g. shifting the propagation direction of the beam, its focal position(s) in propagation direction or transverse distribution.

The analysis of the light field behind the biconvex droplet lenses holds the potential to gain various different and even typically "invisible" information on the properties of droplets on liquid-repelling surfaces and the phenomena influencing these properties. For instance, for droplet lenses on a Taro leaf, the droplet volume affects the liquid lens curvatures and also the propagation distance of light through the lens, which, in turn, also effects the focal intensity structure. Another crucial droplet property, which defines the output intensity distribution, is the refractive index of the liquid. While the droplet shape can be determined from standard camera images, the refractive index is an invisible property for the camera, but could be obtained from the 3D intensity structure shaped by the droplet lens. Furthermore, for Leidenfrost droplets, besides detecting its bouncing behavior, for larger volumes even its shape oscillation in the horizontal plane [52] could be observed. Beyond, invisible properties as its internal flow dynamics [11] could be additionally imprinted into light, as it has been shown by implementing structured light for detecting fluid dynamics [22]. Our approach to analyze the light-shaping features of droplet lenses on liquid-repelling surfaces promise advancement of standard imaging techniques to enable the full decoding of droplet properties by implementing structured light as information carrier.

Funding. Deutsche Forschungsgemeinschaft (DE 486/23-1); Marie Sklodowska-Curie Actions (ColOpt ITN 721465); University of Muenster; Muenster University of Applied Science.

Acknowledgments. The authors acknowledge initial experimental support by Inmaculada Pérez Pérez in investigating shaping light by Leidenfrost droplets. Further, the authors thank Dr. Carmelo Rosales Guzmán for valuable

Optics EXPRESS

discussions, Dr. Birk Andreas for support with respect to the numerical approach, as well as Dr. Dennise Stefan Bauer and the Institute for Evolution and Biodiversity of Plants, University of Muenster, for providing the *Colocasia esculenta* sample.

Disclosures. The authors declare no conflicts of interest.

Data availability. Data underlying the results presented in this paper are not publicly available at this time but may be obtained from the authors upon reasonable request.

References

1. C. Hao, Y. Liu, X. Chen, J. Li, M. Zhang, Y. Zhao, and Z. Wang, "Bioinspired interfacial materials with enhanced drop mobility: From fundamentals to multifunctional applications," Small **12**(14), 1825–1839 (2016).
2. P. Zhang and F. Y. Lv, "A review of the recent advances in superhydrophobic surfaces and the emerging energy-related applications," Energy **82**, 1068–1087 (2015).
3. R. N. Wenzel, "Surface roughness and contact angle ind," Eng. Chem. **28**, 988–994 (1936).
4. A. B. D. Cassie and S. Baxter, "Wettability of porous surfaces," Trans. Faraday Soc. **40**, 546–551 (1944).
5. R. Blossey, "Self-cleaning surfaces – virtual realities," Nat. Mater. **2**(5), 301–306 (2003).
6. M. Kumar and R. Bhardwaj, "Wetting characteristics of Colocasia esculenta (Taro) leaf and a bioinspired surface thereof," Sci. Rep. **10**(1), 1–15 (2020).
7. S. Qiao, S. Li, Q. Li, B. Li, K. Liu, and X.-Q. Feng, "Friction of droplets sliding on microstructured superhydrophobic surfaces," Langmuir **33**(47), 13480–13489 (2017).
8. S. Munekata, "Fluoropolymers as coating material," Prog. Org. Coatings **16**(2), 113–134 (1988).
9. S. Yuan, S. Pehkonen, B. Liang, Y. Ting, K. Neoh, and E. Kang, "Superhydrophobic fluoropolymer-modified copper surface via surface graft polymerisation for corrosion protection," Corros. Sci. **53**(9), 2738–2747 (2011).
10. J. G. Leidenfrost, *De aquae communis nonnullis qualitatibus tractatus* (Ovenius, 1756).
11. A. Bouillant, T. Mouterde, P. Bourrianne, A. Lagarde, C. Clanet, and D. Quéré, "Leidenfrost wheels," Nat. Phys. **14**(12), 1188–1192 (2018).
12. C.-C. Cheng, C. A. Chang, and J. A. Yeh, "Variable focus dielectric liquid droplet lens," Opt. Express **14**(9), 4101–4106 (2006).
13. C. B. Gorman, H. A. Biebuyck, and G. M. Whitesides, "Control of the shape of liquid lenses on a modified gold surface using an applied electrical potential across a self-assembled monolayer," Langmuir **11**(6), 2242–2246 (1995).
14. G. Zhou, A. Yang, Y. Wang, G. Gao, A. Pei, X. Yu, Y. Zhu, L. Zong, B. Liu, J. Xu, N. Liu, J. Zhang, Y. Li, L.-W. Wang, H. Y. Hwang, M. L. Brongersma, S. Chu, and Y. Cu, "Electrotunable liquid sulfur microdroplets," Nat. Commun. **11**(1), 606 (2020).
15. T. Huhtamäki, X. Tian, J. T. Korhonen, and R. H. Ras, "Surface-wetting characterization using contact-angle measurements," Nat. Protoc. **13**(7), 1521–1538 (2018).
16. J. Drelich, "Guidelines to measurements of reproducible contact angles using a sessile-drop technique," Surf. Innov. **1**(4), 248–254 (2013).
17. E. Pierce, F. Carmona, and A. Amirfazli, "Understanding of sliding and contact angle results in tilted plate experiments," Colloids Surfaces A: Physicochem. Eng. Aspects **323**(1-3), 73–82 (2008).
18. M. A. J. van Limbeek, M. H. Klein Schaarsberg, B. Sobac, A. Rednikov, C. Sun, P. Colinet, and D. Lohse, "Leidenfrost drops cooling surfaces: theory and interferometric measurement," J. Fluid Mech. **827**, 614–639 (2017).
19. H. Rubinsztein-Dunlop, A. Forbes, M. V. Berry, M. R. Dennis, D. L. Andrews, M. Mansuripur, C. Denz, C. Alpmann, P. Banzer, T. Bauer, E. Karimi, L. Marrucci, M. Padgett, M. Ritsch-Marte, N. M. Litchinitser, N. P. Bigelow, C. Rosales-Guzmán, A. Belmonte, J. P. Torres, T. W. Neely, M. Baker, R. Gordon, A. B. Stilgoe, J. Romero, A. G. White, R. Fickler, A. E. Willner, G. Xie, B. McMorran, and A. M. Weiner, "Roadmap on structured light," J. Opt. **19**(1), 013001 (2017).
20. A. Forbes, M. de Oliveira, and M. R. Dennis, "Structured light," Nat. Photonics **15**(4), 253–262 (2021).
21. E. Otte, *Structured Singular Light Fields* (Springer, 2021).
22. A. Belmonte, C. Rosales-Guzmán, and J. P. Torres, "Measurement of flow vorticity with helical beams of light," Optica **2**(11), 1002–1005 (2015).
23. M. P. Lavery, F. C. Speirits, S. M. Barnett, and M. J. Padgett, "Detection of a spinning object using light's orbital angular momentum," Science **341**(6145), 537–540 (2013).
24. M. Berry and C. Upstill, *Catastrophe Optics: Morphologies of Caustics and Their Diffraction Patterns* (Elsevier, 1980), vol. 18 of *Progress in Optics*, chap. 4, pp. 257–346.
25. J. F. Nye, "The catastrophe optics of liquid drop lenses," Proc. R. Soc. Lond. A **403**(1824), 1–26 (1986).
26. F. R. A. Onofri, K. F. Ren, M. Sentis, Q. Gaubert, and C. Pelcé, "Experimental validation of the vectorial complex ray model on the inter-caustics scattering of oblate droplets," Opt. Express **23**(12), 15768–15773 (2015).
27. H. Yu, F. Xu, and C. Tropea, "Spheroidal droplet measurements based on generalized rainbow patterns," J. Quant. Spectrosc. Radiat. Transf. **126**, 105–112 (2013). Lasers and interactions with particles 2012.
28. H. Yu, F. Xu, and C. Tropea, "Optical caustics associated with the primary rainbow of oblate droplets: simulation and application in non-sphericity measurement," Opt. Express **21**(22), 25761–25771 (2013).
29. A. Malyuk and N. Ivanova, "Biomimetic liquid lenses actuated by a laser beam: effects of evaporation and orientation to gravity," Mol. Syst. Des. Eng. **5**(7), 1290–1298 (2020).

Optics EXPRESS

30. C. Neinhuis and W. Barthlott, "Characterization and distribution of water-repellent, self-cleaning plant surfaces," Annals of Botany **79**(6), 667–677 (1997).
31. J. Park, J. Park, H. Lim, and H.-Y. Kim, "Shape of a large drop on a rough hydrophobic surface," Phys. Fluids **25**(2), 022102 (2013).
32. A. Sanyal, S. Basu, and R. Kumar, "Experimental analysis of shape deformation of evaporating droplet using Legendre polynomials," Phys. Lett. A **378**(5-6), 539–548 (2014).
33. J. De Ruiter, R. Lagraauw, D. Van Den Ende, and F. Mugele, "Wettability-independent bouncing on flat surfaces mediated by thin air films," Nat. Phys. **11**(1), 48–53 (2015).
34. B. Andreas, G. Mana, and C. Palmisano, "Vectorial ray-based diffraction integral," J. Opt. Soc. Am. A **32**(8), 1403–1424 (2015).
35. B. Andreas, G. Mana, and C. Palmisano, "Vectorial ray-based diffraction integral: erratum," J. Opt. Soc. Am. A **33**(4), 559–560 (2016).
36. B. Andreas, "Vectorial ray-based diffraction integral (VRBDI)," MathWorks® File Exchange, http://nl.mathworks.com/matlabcentral/fileexchange/52210-vectorial-ray-based-diffraction-integral-vrbdi.
37. D. Bonn, J. Eggers, J. Indekeu, J. Meunier, and E. Rolley, "Wetting and spreading," Rev. Mod. Phys. **81**(2), 739–805 (2009).
38. C. Frankiewicz and D. Attinger, "Texture and wettability of metallic lotus leaves," Nanoscale **8**(7), 3982–3990 (2016).
39. N. D. Patil, R. Bhardwaj, and A. Sharma, "Droplet impact dynamics on micropillared hydrophobic surfaces," Exp. Therm. Fluid Sci. **74**, 195–206 (2016).
40. K. Koch and W. Barthlott, "Superhydrophobic and superhydrophilic plant surfaces: an inspiration for biomimetic materials," Phil. Trans. R. Soc. A. **367**(1893), 1487–1509 (2009).
41. C. Extrand and S. I. Moon, "Contact angles of liquid drops on super hydrophobic surfaces: Understanding the role of flattening of drops by gravity," Langmuir **26**(22), 17090–17099 (2010).
42. V. A. Lubarda and K. A. Talke, "Analysis of the equilibrium droplet shape based on an ellipsoidal droplet model," Langmuir **27**(17), 10705–10713 (2011).
43. G. Whyman and E. Bormashenko, "Oblate spheroid model for calculation of the shape and contact angles of heavy droplets," J. Colloid Interface Sci. **331**(1), 174–177 (2009).
44. S. van der Walt, J. L. Schönberger, J. Nunez-Iglesias, F. Boulogne, J. D. Warner, N. Yager, E. Gouillart, and T. Yu, "scikit-image: image processing in Python.," PeerJ. **2**, e453 (2014).
45. S. Wciślik, "Thermal infrared mapping of the Leidenfrost drop evaporation," in *Journal of Physics: Conference Series*, vol. 745 (IOP Publishing, 2016), p. 032064.
46. G. Wang, J. R. McDonough, V. Zivkovic, T. Long, and S. Wang, "From thermal energy to kinetic energy: Droplet motion triggered by the Leidenfrost effect," Adv. Mater. Interfaces **8**, 2001249 (2021).
47. G. Graeber, K. Regulagadda, P. Hodel, C. Küttel, D. Landolf, T. M. Schutzius, and D. Poulikakos, "Leidenfrost droplet trampolining," Nat. Commun. **12**(1), 1727 (2021).
48. L. Ulahannan, K. Krishnakumar, A. R. Nair, and S. K. Ranjith, "An experimental study on the effect of nanoparticle shape on the dynamics of Leidenfrost droplet impingement," Exp. Comput. Multiph. Flow **3**(1), 47–58 (2021).
49. D. Liu and T. Tran, "Size-dependent spontaneous oscillations of Leidenfrost droplets," J. Fluid Mech. **902**, A21 (2020).
50. P. Bourrianne, C. Lv, and D. Quéré, "The cold Leidenfrost regime," Sci. Adv. **5**(6), 1 (2019).
51. T. R. Cousins, R. E. Goldstein, J. W. Jaworski, and A. I. Pesci, "A ratchet trap for Leidenfrost drops," J. Fluid Mech. **696**, 215–227 (2012).
52. N. J. Holter and W. R. Glasscock, "Vibrations of evaporating liquid drops," The J. Acoust. Soc. Am. **24**(6), 682–686 (1952).